Wideband Linearization of a Carrier Aggregation Transmitter Using Analog Signal Injection and 2-D Digital Predistortion

Nimrod Ginzberg, *Graduate Student Member, IEEE*, Tomer Gidoni,

Yanir Schwartz, and Emanuel Cohen, *Member, IEEE*

Abstract—We introduce a transmitter (TX) architecture and a linearization technique for concurrent transmission of two intraband noncontiguous carrier aggregation signals in the 5 GHz frequency band. The technique is based on low-power and narrowband analog signal injection to compensate for out-of-band (OOB) third-order intermodulation distortions (IMD3), together with 2-D digital predistortion to address error vector magnitude (EVM) degradation caused by in-band intermodulation and cross-modulation distortions. The hybrid analog-digital design enables wideband linearization over the entire third-order distortion bandwidth (BW) using practical sampling rate requirements from the digital-to-analog converter (DAC) and analog-to-digital converter (ADC). The system's performance was evaluated using a class AB power amplifier implemented in the 180 nm CMOS technology and two VHT 802.11ac Wi-Fi signals with a 20 MHz modulation BW. The linearization technique achieves 7–12 dB cancellation of OOB IMD3 products along with 6–9 dB of in-band EVM correction at 8 dBm average output power over a BW of up to 1.2 GHz, with only 60 MHz BW requirement from the DACs and ADCs.

Index Terms—Carrier aggregation (CA), compensation signal injection, intermodulation distortion (IMD), linearization, power amplifier, 2-D digital predistortion (DPD).

I. INTRODUCTION

THE growing demand for high-data-rate transmission in modern wireless communication systems has motivated the development of broadband wireless technologies to support increased channel capacity. A distinct feature in such systems is carrier aggregation (CA)–a configuration in which two or more component carriers are aggregated on the physical layer to support wider transmission bandwidths (BWs). CA allows for concurrent transmission across multiple carriers in the same band or in different bands to provide maximum flexibility in utilizing the available radio spectrum.
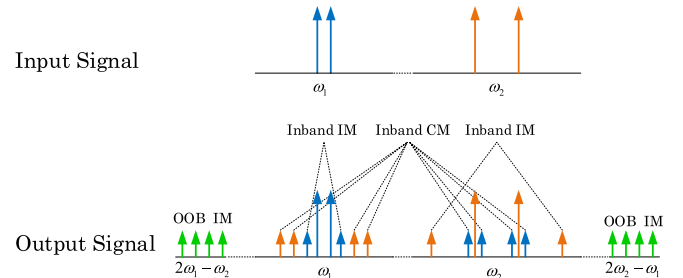
Fig. 1. Power spectrum of a concurrent two-tone TX.

The performance of CA TXs processing two or more channels is significantly restricted by nonlinear effects, resulting in the appearance of undesired intermodulation distortion (IMD) products at the TX output [1]. IMD may be caused by in-band intermodulation within the channels themselves [e.g., in multicarrier modulation such as orthogonal frequency-division multiplexing (OFDM)], in-band cross modulation (CM) between the different channels and out-of-band (OOB) emissions arising from intermodulation between the different channels. Fig.1 shows the three types of distortion terms at the output of a concurrent dual-band nonlinear TX.

Several techniques may be employed to address the distortions in two-channel CA TXs. The 2-D digital predistortion (2D-DPD) schemes that improve both in-band and OOB IMD, implemented in various single-antenna CA TX architectures, have been reported. In [2]–[7], the TX employed pre-PA combining of two narrowband digital-to-analog converters (DACs) [Fig. 2-(a1)] and the 2D-DPD focused on in-band linearization only due to the limited sampling rates of the instrumentation [narrowband DPD in Fig. 2(b)]. Work [8] addressed OOB distortions by direct harmonic injection of correction signals at the third-order IMD (IMD3) frequencies, but their approach required additional DACs and analog-to-digital converters (ADCs). Works [9]–[14] implemented pre-PA combining using wideband DAC and 2D-DPD [Fig. 2-(a2) and wideband DPD in Fig. 2(b)] that covered the entire third-order distortion BW, which may become impractical for widely spaced carriers.

The TX architecture and the linearization technique proposed in this article, shown in Fig. 2-(a3), aim to exploit
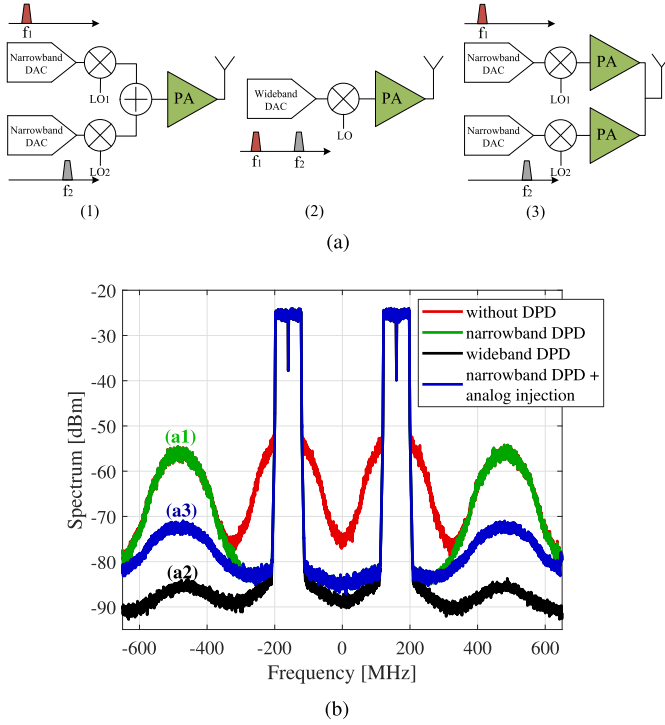
Fig. 2. (a) Different architectures for the aggregation of two carriers. (a1) Narrowband pre-PA combining, (a2) wideband pre-PA combining, and (a3) post-PA combining (this article). (b) Spectrum of (a1) and (a2) with narrowband and wideband 2D-DPD, respectively, and spectrum of (a3) with narrowband 2D-DPD and analog injection.

the benefits of configurations (a1) and (a2) in Fig. 2(a), that is, achieving wideband suppression of in-band and OOB distortions using narrowband DACs and DPD [narrowband DPD and analog injection in Fig. 2(b)]. In-band distortion is dealt with digitally using narrowband 2D-DPD, whereas OOB IMD3 cancellation is performed in the analog domain by employing a new compensation technique of in-band signal injection. The two channels are combined at the output (post-PA combining) and transmitted through a single antenna. By using the existing PAs that form the TX as the nonlinear source to generate the canceling terms at the OOB IMD3 frequencies, no additional circuitry blocks nor complex analog schemes, as in [15]–[20], are required. The resulting TX allows for flexible spectrum utilization, independent of the signals' BW and the frequency separation between them. Table I compares the properties of the different CA TX architectures.

This article exploits the high output impedance property of the PAs reported in [21] to minimize TX losses due to mutual loading in a CA operation mode. In [22], we demonstrated the analog compensation technique for continuous-wave (CW) signals. In this article, we propose a comprehensive theoretical analysis of the linearization technique and present extensive measurement results that support it using two widely spaced intraband OFDM signals.

II. PROPOSED SIGNAL INJECTION TECHNIQUE

The linearization scheme proposed in this article is shown in Fig. 3. The TX comprises two PAs that are connected in parallel to a single antenna. The IMD3 cancellation is achieved

TABLE I
CA TX ARCHITECTURES COMPARISON

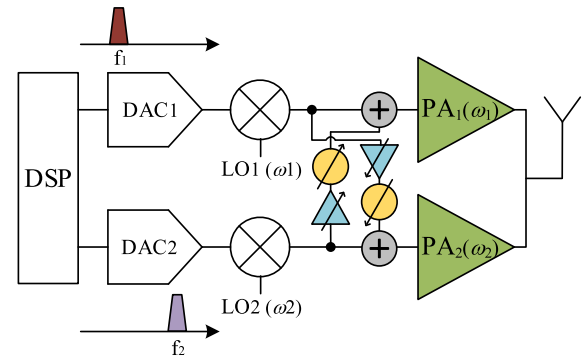| Transmitter	Pros	Cons
Narrowband pre-PA combining Fig. 2-(a1)	Narrowband DAC and DPD	Uncompensated OOB IMD3
Wideband pre-PA combining Fig. 2-(a2)	OOB IMD3 compensation	Wideband DAC and DPD
Narrowband post-PA combining (this work) Fig. 2-(a3)	OOB IMD3 compensation Narrowband DAC and DPD	Mutual PA loading

Fig. 3. Proposed TX architecture and compensation technique. The compensation signal injected to PA_1 is an attenuated and phased shifted replica of the signal at PA_2.
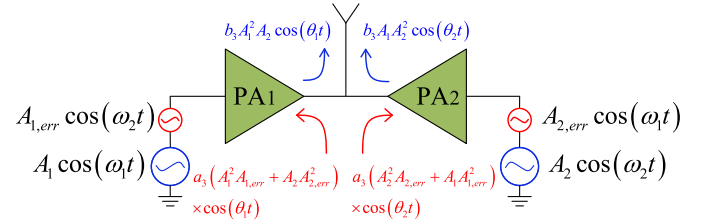

Fig. 4. Illustration of the compensation technique operation principle. The existing PAs that form the TX are used as the nonlinear source to generate the canceling terms at the OOB IMD3 frequencies.

by injecting low power compensation signals to the inputs of the PAs in the following method: the compensation signal injected to PA_i is an attenuated and phase-shifted replica of the signal at PA_j ($i, j \in \{1, 2\}, i \neq j$) such that the nonlinearity at the PA input is utilized to generate the canceling IMD3 terms at the output, as shown in Fig. 4. Note that this technique is inapplicable to the pre-PA combining architectures, as will be explained in detail in Section II-D.

Since the cancellation signals are in-band, no additional BW is required from the DAC, and the compensation is limited neither by the channel BW nor by the frequency separation between the carriers. In addition, the nonlinearity that generates IMD3 in the proposed architecture is fundamentally weaker than that of a single two-tone PA since the nonlinear

gain is a weaker function of the output voltage v_{ds} than of the input voltage v_{gs} [15]. This observation allows for the injection of relatively low-power compensation signals with respect to the input signals' power level.

The canceling signals are equalized based on frequency-flat attenuated and phase-shifted replica of the input signals, as shown in Fig. 3. Consequently, a narrowband phase and amplitude variation range is sufficient, and linearity requirement from the attenuator and the phase shifter can be considerably relaxed since they process small-signal power levels. Moreover, as the cancellation target is in the order of 10 dB, as will be shown in Sections II-C and IV-C, the control accuracy is about 15° in phase and 25% in amplitude, which is a moderate design requirement.

The TX nonlinearity can be modeled using a Taylor series expansion of the drain current I_{ds} with respect to two control voltages V_{gs} and V_{ds} [23]. Ignoring zero and second-order derivatives, which do not contribute IMD3 terms, the series expansion takes the form

$$I_{ds}(V_{gs}, V_{ds}) = \frac{\partial I_{ds}}{\partial V_{gs}} v_{gs} + \frac{\partial I_{ds}}{\partial V_{ds}} v_{ds}$$
$$+ \frac{1}{6} \frac{\partial^3 I_{ds}}{\partial V_{gs}^3} v_{gs}^3 + \frac{1}{2} \frac{\partial^3 I_{ds}}{\partial^2 V_{gs} \partial V_{ds}} v_{gs}^2 v_{ds}$$
$$+ \frac{1}{2} \frac{\partial^3 I_{ds}}{\partial V_{gs} \partial^2 V_{ds}} v_{gs} v_{ds}^2 + \frac{1}{6} \frac{\partial^3 I_{ds}}{\partial V_{ds}^3} v_{ds}^3 \quad (1)$$

where v_{gs} and v_{ds} are the deviations from V_{gs} and V_{ds}, respectively. The small-signal current can be written as

$$i_{ds}(v_{gs}, v_{ds}) = G_m v_{gs} + G_{m3} v_{gs}^3$$
$$+ G_{m2d} v_{gs}^2 v_{ds} + G_{md2} v_{gs} v_{ds}^2$$
$$+ G_{d3} v_{ds}^3 + G_{ds} v_{ds} \quad (2)$$

where the various coefficients are the corresponding derivatives of (1).

Let $v_{gs1} = A_1 \cos(\omega_1 t)$ and $v_{gs2} = A_2 \cos(\omega_2 t)$ be two sinusoidal signals applied to the input of PA$_1$ and PA$_2$, respectively, where A_1 and A_2 are the signals' amplitudes and ω_1 and ω_2 are angular frequencies. For simplicity, we assume a linear relation between v_{gs} and v_{ds}, i.e., $v_{ds} = G_m(v_{gs1} + v_{gs2}) R_{out}$. The signals' interaction through the nonlinearity in (2) gives rise to the IMD3 components at the frequencies $\Omega_1 = 2\omega_1 - \omega_2$ and $\Omega_2 = 2\omega_2 - \omega_1$

$$i_{out}(t)_{(\Omega_1)} = b_3 A_1^2 A_2$$
$$i_{out}(t)_{(\Omega_2)} = b_3 A_1 A_2^2 \quad (3)$$

where $b_3 = (1/4) G_m R_{out} (G_{m2d} + 3 G_{md2} G_m R_{out} + 3 G_{d3} G_m^2 R_{out}^2)$, that is, $i_{out}(t)_{(\Omega_i)}$, the current at the output in each IMD3 component, is a function of the corresponding frequency Ω_i and the input amplitudes. b_3 is a coefficient expressing the third-order nonlinearity at the output, and it is a function of amplifier-dependent parameters.

To eliminate the IMD3 terms in (3), two compensation signals, $A_{1,err} \cos(\omega_2 t)$ and $A_{2,err} \cos(\omega_1 t)$, are injected to the inputs of PA$_1$ and PA$_2$, respectively, where $A_{1,err}$ and $A_{2,err}$ are the unknown complex correction amplitudes to be calculated. Assuming that the nonlinear gain is mainly dominated by the input nonlinearity (i.e., $G_{m3} \gg G_{m2d}, G_{md2}, G_{d3}$ [15]), and that the compensation signals are relatively small, the new IMD3 terms that emerge at the output are given based on (2)

$$i_{out,err}(t)_{(\Omega_1)} = a_3 (A_1^2 A_{1,err} + A_2 A_{2,err}^2)$$
$$i_{out,err}(t)_{(\Omega_2)} = a_3 (A_2^2 A_{2,err} + A_1 A_{1,err}^2) \quad (4)$$

where $a_3 = (3/4) G_{m3}$. a_3 represents the input-referred nonlinearity, and it is also an amplifier-dependent parameter. The combined output current at Ω_1 is therefore

$$i_{out,tot}(t)_{(\Omega_1)} = i_{out}(t)_{(\Omega_1)} + i_{out,err}(t)_{(\Omega_1)}$$
$$= b_3 A_1^2 A_2 + a_3 (A_1^2 A_{1,err} + A_2 A_{2,err}^2) \quad (5)$$

and similarly for Ω_2

$$i_{out,tot}(t)_{(\Omega_2)} = b_3 A_1 A_2^2 + a_3 (A_2^2 A_{2,err} + A_1 A_{1,err}^2). \quad (6)$$

To obtain IMD3 cancellation, we demand that $i_{out,tot}(\Omega_i) = 0$ for $i = 1, 2$, which entails finding appropriate correction amplitudes, $A_{1,err}$ and $A_{2,err}$, such that

$$\begin{cases} b_3 A_1^2 A_2 = -a_3 (A_1^2 A_{1,err} + A_2 A_{2,err}^2) \\ b_3 A_1 A_2^2 = -a_3 (A_2^2 A_{2,err} + A_1 A_{1,err}^2). \end{cases} \quad (7)$$

The required correction amplitudes are obtained from the solution of (7)

$$A_{1,err} = -\frac{A_2}{2} \left(1 \pm \sqrt{1 - 4\frac{b_3}{a_3}} \right)$$
$$A_{2,err} = -\frac{A_1}{2} \left(1 \pm \sqrt{1 - 4\frac{b_3}{a_3}} \right). \quad (8)$$

The power ratio between the main signals and the correction signals depends on the magnitude ratio between the input and output nonlinearities, represented by a_3 and b_3, respectively.

A. Effect of Cancellation on the In-Band Power

To evaluate the effect of cancellation on the in-band power, we substitute (8) into (2). Assuming that in the linear region of operation, the gain is dominated by G_m, the output current at the fundamental frequencies is given by

$$i_{out}(t)_{(\omega_1)} \approx G_m(A_1 + A_{2,err}) = G_m \frac{A_1}{2} \left(1 \mp \sqrt{1 - 4\frac{b_3}{a_3}} \right)$$
$$i_{out}(t)_{(\omega_2)} \approx G_m(A_2 + A_{1,err}) = G_m \frac{A_2}{2} \left(1 \mp \sqrt{1 - 4\frac{b_3}{a_3}} \right). \quad (9)$$

The appropriate sign of the square root term is made clear with a first-order Taylor expansion of $i_{out}(t)_{(\omega_i)}$. Under the assumption that $a_3 \gg b_3$, (9) can be written as

$$i_{out,i}(t)_{(\omega_i)} \approx G_m \frac{A_i}{2} \left(1 \mp \left(1 - 2\frac{b_3}{a_3} \right) \right)$$
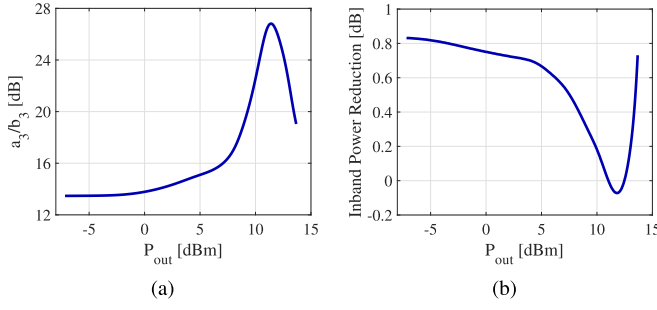$$= \begin{cases} G_m A_i \dfrac{b_3}{a_3}, & \text{(a)} \\ \\ G_m A_i \left(1 - \dfrac{b_3}{a_3} \right), & \text{(b)} \end{cases} \quad (10)$$

Fig. 5.   (a) Simulated third-order coefficient ratio a_3/b_3 and (b) its impact on the in-band output power.

Fig. 6.   Third-order coefficient ratio a_3/b_3 and output power as a function of the gate bias voltage for -8 dBm input power.

where $i = 1, 2$. The valid solution is 10(b), and it describes the impact of cancellation on the output power as follows:

$$P_{\text{out},(\omega_1)} \propto \text{dB}_{20}\left[i_{\text{out},1}(t)_{(\omega_1)} \right] \approx \text{dB}_{20}\left[G_m A_1 \left(1 - \frac{b_3}{a_3} \right) \right]$$

$$P_{\text{out},(\omega_2)} \propto \text{dB}_{20}\left[i_{\text{out},2}(t)_{(\omega_2)} \right] \approx \text{dB}_{20}\left[G_m A_2 \left(1 - \frac{b_3}{a_3} \right) \right]. \quad (11)$$

Evidently, the stronger the input-referred third-order nonlinear coefficient a_3 compared with the output-referred third-order nonlinear coefficient b_3, the smaller the penalty in P_{out} resulting from the injection of the cancellation signals.

B. Nonlinearity Magnitude Ratio a_3/b_3

The ability of the proposed signal injection technique to effectively compensate for OOB IMD3 while imposing minimal degradation to the in-band output power depends on the third-order nonlinearity magnitude ratio between the postcombined system, designated as b_3, and the single PA as a standalone device, designated as a_3, as implied from (11). A fundamental nonlinear mechanism present at the input of the PA is the nonlinear gate capacitance, $C_{\text{gs}}[v_{\text{gs}}(t)]$, which gives rise to a nonlinear gate current of the form [24]

$$i_{\text{gs}}(t) = C_{\text{gs}}[v_{\text{gs}}(t)]\frac{dv_{\text{gs}}(t)}{dt} \quad (12)$$

where $C_{\text{gs}}[v_{\text{gs}}(t)] = (C_0 + C_1 \cdot v_{\text{gs}} + C_2 \cdot v_{\text{gs}}^2 + C_3 \cdot v_{\text{gs}}^3 + \cdots)$ and $C_n (n = 1, 2, 3, \ldots)$ are bias-dependent coefficients.

The nonlinear gate current contributes to the OOB IMD3 terms by mixing the two-tone input signal, $A_i(\cos\omega_i) + A_{i,\text{err}}\cos(\omega_j)$, $i, j \in \{1, 2\}, i \neq j$, through the input-referred nonlinearity. Therefore, this gate capacitance's nonlinearity manifests itself in the a_3 coefficient, in addition to the i_{ds} nonlinearity described in (1), but it is not present in the b_3 coefficient. As a result, b_3 is fundamentally weaker than a_3, allowing to compensate for IMD3 while having a low impact on the in-band output power.

Fig. 5 shows the simulation results of the magnitude ratio between a_3 and b_3 for the PA described in Section III. The coefficients were obtained by fitting the output current to the polynomial model in (2), and the impact on the in-band output power was calculated according to (9). The simulation results show that the a_3/b_3 ratio increases with P_{out} up to a peak at 11 dBm [see Fig. 5(a)]. The small gain observed at this power level is attributed to the phase of a_3/b_3, which, in some cases,
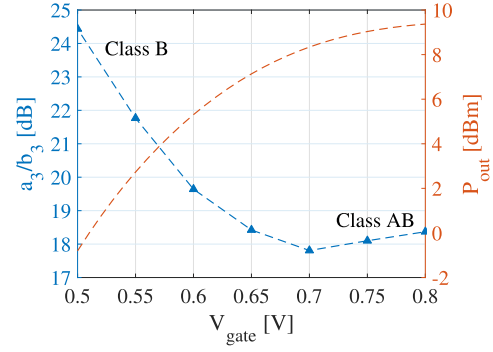
may result in a power summation of the correction signal and the main signal. Although, for low output powers, the in-band power loss is more pronounced [see Fig. 5(b)], the IMD3 terms are small, and compensation is less crucial.

The observation that the input gate capacitance has a significant contribution to a_3 can have implications on the design guidelines of the PA. PA classes with lower gate bias voltages may have stronger gate nonlinearity compared with a class AB-PA, as validated in simulation, however, at the account of lower gain (see Fig. 6).

C. Cancellation Limit

The amplitude and phase signals, representing the two degrees of freedom in the IMD cancellation in (8), are chosen so as to eliminate the third-order nonlinearities with a spectral envelope of the form $A_i^2 A_j$ $(i, j \in \{1, 2\}, i \neq j)$. However, when considering higher order nonlinearities, new terms with different spectral envelope appear at the IMD3 frequencies. Taking the next odd-order nonlinearity into account, the output current at Ω_i also includes the fifth-order terms [25]

$$i_{\text{out}}(t)_{(\Omega_i)} = b_3 A_i^2 A_j + \frac{15}{8}b_5 A_i^2 A_j^3 + \frac{5}{4}b_5 A_i^4 A_j. \quad (13)$$

Assuming that the compensation signals fully eliminate the third-order contribution to the IMD3 terms, the cancellation is now limited by the fifth-order nonlinearity, and (13) now reads

$$i_{\text{out}}(t)_{(\Omega_i)} = \frac{15}{8}b_5 A_i^2 A_j^3 + \frac{5}{4}b_5 A_i^4 A_j. \quad (14)$$

The cancellation limit can be evaluated from the ratio between the fifth-order intermodulation distortion (IMD5) terms and the remaining IMD3 terms consisting of the uncompensated fifth-order contributions. The IMD5 terms arising from introducing a fifth-order term b_5 to the current polynomial are given by

$$i_{\text{out}}(t)_{(3\omega_i - 2\omega_j)} = \frac{5}{8}b_5 A_i^2 A_j^3. \quad (15)$$

For $|A_i| = |A_j|$, the lowest achievable level of the compensated IMD3 will always be higher than the level of the

IMD5 by the ratio between (14) and (15)

$$\frac{\hat{i}_{\text{out,min}}(\Omega_i)}{\hat{i}_{\text{out}}(3\omega_i - 2\omega_j)} > \frac{\sqrt{(15/8)^2 + (5/4)^2}}{(5/8)} \approx 11 \text{ dB}. \quad (16)$$

The system's measurements indicate that IMD3 cancellation is indeed limited to 7–12 dB (see Figs. 20 and 21), depending on various factors, such as signal power and frequency separation between the channels.

In the CW case, several simplifying assumptions can be made based on the derivation thus far. According to (8), the compensation signals can be expressed as

$$A_{1,\text{err}} = \alpha A_2$$
$$A_{2,\text{err}} = \beta A_1 \quad (17)$$

where α and β are complex coefficients and $|\alpha|, |\beta| < 1$. If assuming, for simplicity, $A_1 = A_2 = A$, where A is the signal's amplitude (which is merely a number in this case), (13) then takes the form

$$\hat{i}_{\text{out}}(\Omega_i) = b_3 A^3 + \widetilde{b}_5 A^5 \quad (18)$$

where $\widetilde{b}_5 = (25/8)b_5$. Substituting (17) and (18) into (7) yields

$$\begin{cases} b_3 A^3 + \widetilde{b}_5 A^5 = -a_3 A^3(\alpha + \beta^2) \\ b_3 A^3 + \widetilde{b}_5 A^5 = -a_3 A^3(\beta + \alpha^2). \end{cases} \quad (19)$$

The solution for (19) that satisfies $|\alpha|, |\beta| < 1$ is given by

$$\alpha = \beta = \sqrt[3]{-\frac{b_3 + \widetilde{b}_5 A^2}{a_3}}. \quad (20)$$

Following (20), in the case of CW signals, all the nonlinear orders of the output current collapse into a single complex constant, which can be counteracted with a proper selection of the compensation signal coefficients according to (20). The abovementioned derivation can be generalized to include any higher order nonlinearities, as well as different amplitudes of the main signals.

D. OOB IMD3 Cancellation Using a Single PA

It is constructive to examine a configuration in which we give up one of the PAs that form the TX and employ the proposed compensation technique to a single precombining PA. For this configuration, the signal at the PA input is as follows

$$v_{\text{in}}(t) = (A_1 + A_{2,\text{err}})\cos(\omega_1 t) + (A_2 + A_{1,\text{err}})\cos(\omega_2 t). \quad (21)$$

The output current at the IMD3 frequencies according to (4) is given by

$$i_{\text{out,err}}(t)_{(\Omega_1)} = a_3(A_1 + A_{2,\text{err}})^2(A_2 + A_{1,\text{err}})$$
$$i_{\text{out,err}}(t)_{(\Omega_2)} = a_3(A_2 + A_{1,\text{err}})^2(A_1 + A_{2,\text{err}}) \quad (22)$$

where $\Omega_1 = 2\omega_1 - \omega_2$ and $\Omega_2 = 2\omega_2 - \omega_1$. To obtain IMD3 cancellation, we demand that $i_{\text{out,err}}(t)_{(\Omega_i)} = 0$, which is accomplished only if $A_1 = -A_{2,\text{err}}$ and/or $A_2 = -A_{1,\text{err}}$. The sheer result of this experiment is that $v_{\text{in}} = 0$, and therefore, $P_{\text{out}} = 0$ for either the two fundamental frequencies in tandem or for one frequency only. According to the latter option, the PA functionality reduces to that of a single-tone TX.
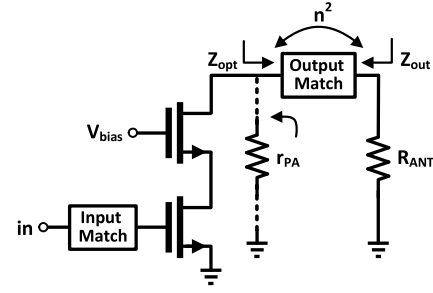

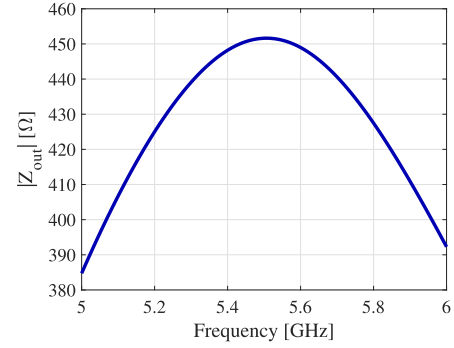Fig. 7.   High output impedance cascode power amplifier.

Fig. 8.   Simulated Z_{out} vs. frequency.

III. CIRCUIT DESIGN AND SIMULATION

A. Design for High Output Impedance

The parallel combining of the two PAs in the postcombining TX [denoted by PC-TX, see Fig. 2-(a3)] dictates a design for the PAs to introduce high output impedance to mitigate mutual PA loading while maintaining the load conditions for maximum power-added efficiency (PAE) and the required P_{sat}. High impedance in parallel with the antenna allows for each PA to operate as if it were a standalone amplifier in terms of the load conditions is sees.

The output impedance magnitude is determined by the PA's drain resistance r_{PA} and the matching network's impedance conversion factor, n^2. For high drain resistance, a cascode topology was chosen (see Fig. 7). Together with the process parameters of the relatively long-channel TSMC 180 nm technology, the bias conditions and the transistor dimensions were selected to achieve $r_{\text{PA}} \approx 800 \ \Omega$ and $R_{\text{opt}} \approx 100 \ \Omega$. The required impedance conversion factor to match R_{opt} to the 50 Ω antenna is $n^2 = 2$. Therefore, the output impedance of the PA, as seen from the antenna, is $|Z_{\text{out}}| \approx 400 \ \Omega$ (see Fig. 8). This translates to $\text{dB}_{10}(50) - \text{dB}_{10}(50||400) \approx 0.5$ dB loss due to mutual loading compared with a single standalone PA (see Fig. 9).

Fig. 9 shows the effect of mutual PA loading on the gain and PAE of the PC-TX, obtained from a two-tone simulation at the frequencies 5.4 and 5.6 GHz. First, the power of PA$_1$ at 5.4 GHz was swept, while PA$_2$ was fed with a low-power input signal at 5.6 GHz. A gain reduction of 0.5 dB at low output powers and a 1 dB loss at compression is observed in the postcombining configuration compared with the standalone PA [see Fig. 9(a)]. Second, the power at both frequencies was
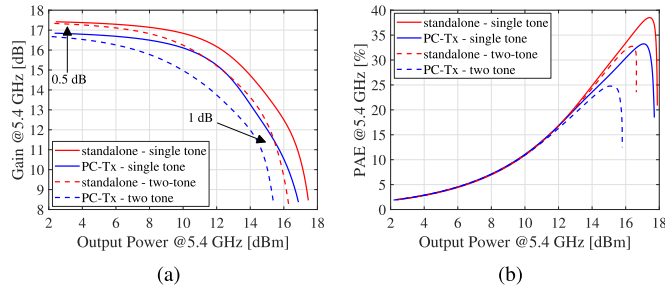
Fig. 9. Loading effect on (a) gain P_{sat} and (b) PAE at different operating power levels.
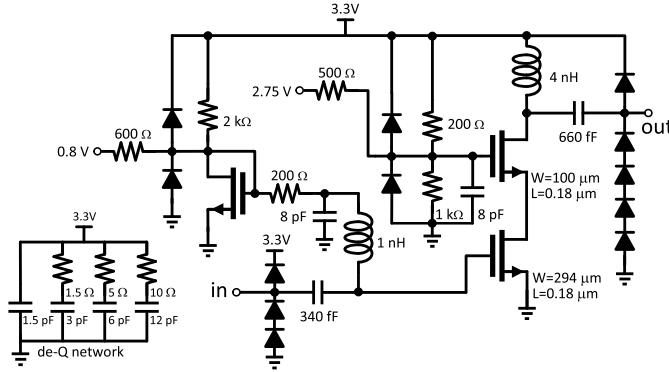

Fig. 10. PA Schematic.

swept in order to evaluate a worst case scenario in which the two signals are at peak power simultaneously. In this test, an additional loss of 1 dB at 4 dB compression point is observed [see Fig. 9(a)]. Nonetheless, as the transmit signals are uncorrelated high peak-to-average power ratio (PAPR) OFDM packets, this scenario is statistically infrequent.

The PA was designed as a class AB cascode using TSMC 180 nm CMOS technology (see Fig. 10) to operate around 5.5 GHz with a BW of 1 GHz, to comply with the IEEE 802.11ac standard for WLAN. The current mirror used for biasing also provides a low impedance node at the bias branch, which is essential for stability. A distributed RC bypass network was placed between the supply and the ground to introduce low impedance at higher harmonics of f_0, alongside with a low Q over a broad range of frequencies to suppress parasitic high-Q shunt resonances and mitigate instability [26]. Input and output impedance matching was implemented using LC networks. Electrostatic discharge (ESD) protection diodes were placed at all nodes interfacing external signals.

B. Post-PA Combining Alternatives

This section discusses two different approaches for post-PA combining: off-chip and on-chip.

1) Off-Chip Combining: According to this approach, each PA is designed as a standalone device, including its output matching network, and is combined off-chip with the other PA on the PCB [see Figs. 11(a) and 16(b)]. In this configuration, the impedance in parallel with the antenna is Z_{out} of the PA after the matching network transformation. Therefore, the load deviates from 50 to (400||50) Ω, resulting in a 0.5 dB loss.
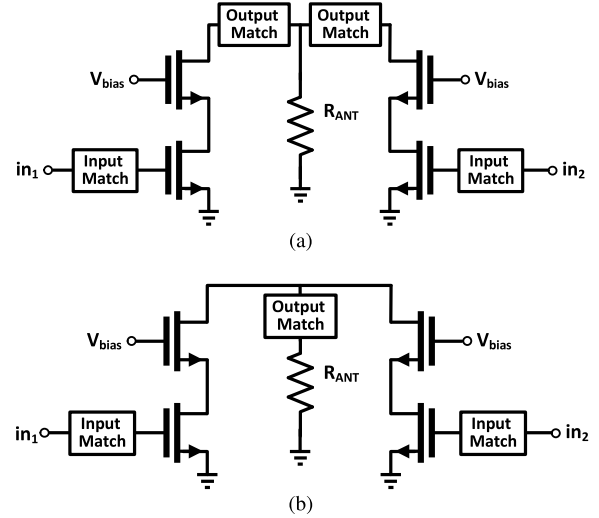

Fig. 11. Post-PA combining option. (a) Off-chip combining. (b) On-chip combining with a shared matching network.
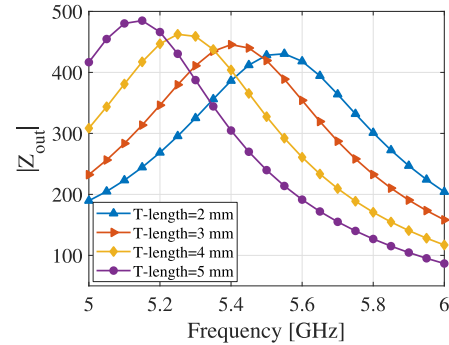

Fig. 12. EM simulation of the output impedance for different lengths of the "T-shaped" transmission line's vertical dimension.

The total size of the TX is larger than that of the on-chip combined TX since each PA consists of an output matching network, which includes an additional inductor, and the packaging requires placement of two dies instead of one. In addition, off-chip combining requires the design of a dedicated "T-shaped" transmission line on the PCB [see Fig. 13(a)] to deliver the outputs of the PAs to the antenna, such that the distance between them (the "T-length") is as small as possible in order to minimize the frequency shift in the peak output impedance (see Fig. 12). It is also noted from Fig. 12 that the transmission line narrows the output impedance magnitude over frequency compared with Fig. 8. Matching and insertion loss of this transmission line, with a 2 mm distance between its horizontal edges, were evaluated in electromagnetic (EM) simulation [see Fig. 13(b)]. Nonetheless, off-chip combining has better linearity compared with on-chip combining due to the loss of the matching network in both PAs, which slightly mitigates the interaction between them. In addition, off-chip connection enables testing of the single PA performance in a probe station. In this article, we have implemented the off-chip combining approach.

2) On-Chip Combining: The two PAs are connected on-chip such that they can share a single output matching network [see Fig. 11(b)]. This may result in a smaller die size since
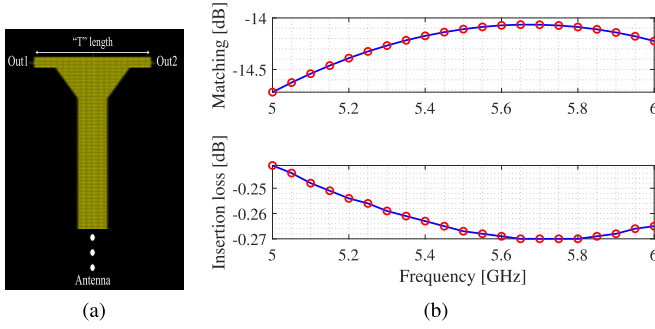
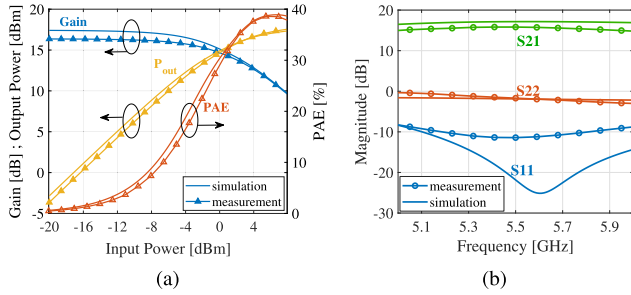Fig. 13. EM simulation of the "T-shaped" transmission line. (a) EM view. (b) Matching and insertion loss.

Fig. 14. Measured and simulated standalone PA. (a) Gain, PAE, and output power and (b) frequency response.

the output matching inductors can be combined in parallel to a single inductor that is roughly half in size. In this configuration, the impedance connected in parallel to the load is r_{PA}, meaning that the load deviates from R_{opt} to $R_{opt}||Z_{out}$, i.e., $(800||100)$ Ω, resulting in the same 0.5 dB loss. Naturally, this approach does not allow to test each PA standalone in a probe station.

IV. MEASUREMENTS

A. Standalone High Output Impedance PA

The standalone PA measurements were performed on-die in a probe station. The PA delivers 17 dBm from a 3.3 V supply at 5.5 GHz with a BW of nearly 1 GHz and achieves a maximum power gain of 16.5 dB and 38% peak PAE (see Fig. 14). The PA's stability factor is >1 at all frequencies (see Fig. 15). The PAs were mounted on a Rogers 4350B PCB for the system measurements. The die micrograph and the PCB are shown in Fig. 16. The total die size is 600 μm × 850 μm.

B. CW Cancellation Measurements

CW measurements were performed at 9 dBm output power. Two channels of a Keysight M8195A 65 GSa/s four-channel arbitrary waveform generator (AWG) transmitted the main signals at 5.3 and 5.7 GHz, and the other two injected the compensation signals, which were combined with the main signals using power combiners. The correction signals' attenuation and phase shift were set directly from the AWG, which enabled a simple control on the delay and amplitude of each channel. The measured results, plotted in Fig. 17(a),
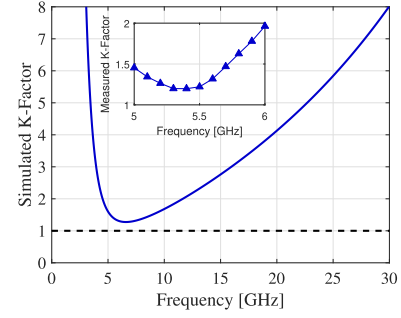

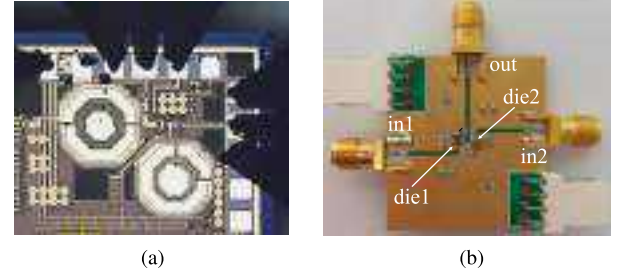Fig. 15. Simulated and measured stability factor.

Fig. 16. (a) PA micrograph. (b) PCB test circuit.

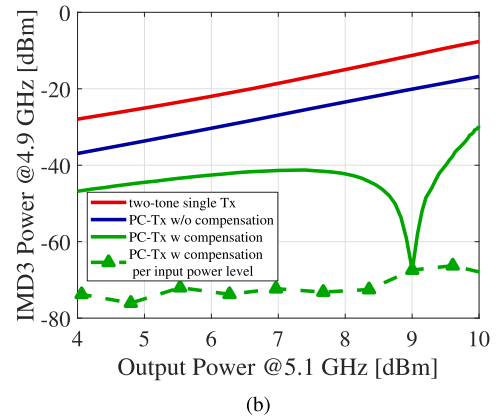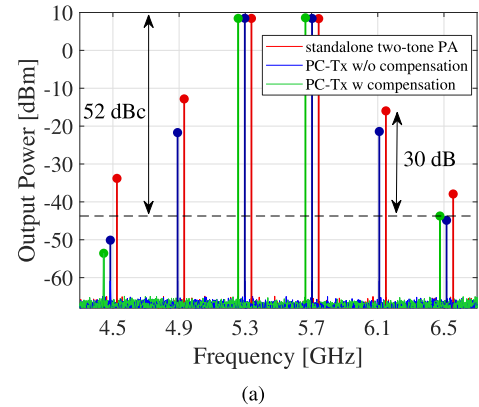Fig. 17. Measured IMD3 cancellation in a two-tone CW test. (a) Cancellation at 9 dBm output power. (b) Cancellation at different output powers.

show that the compensation technique suppresses the OOB IMD3 terms by at least 45 dB such that the strongest spurious emissions are caused by the fifth-order intermodulation products at −52 dBc. In addition, a 30 dB improvement in spurious-free dynamic range (SFDR) is achieved compared

TABLE II

OOB IMD3 SUPPRESSION FOR CW SIGNALS

Source	Method	Circuit Complexity	Center Frequency [GHz]	Frequency Spacing [MHz]	C/I3 [dBc]	ΔC/I3 [dB]	IMD3 BW [MHz]
Fan [19]	Harmonic & Baseband Injection	High	2.1	0.1	60	34	0.3
Chun [15]	Baseband Injection	Medium	1.95	0.1	65	45	0.3
Moazzam [17]	Second Harmonic Feedback	Medium	0.5	1	30	16	3
This Work	RF Injection	Low	5.5	400	77	48	1200

with a standalone two-tone PA. Note that the power of the IMD3 terms in the standalone two-tone PA is indeed higher than that in the postcombining TX, as stated earlier. For a fair comparison, the measurements of the standalone two-tone PA were calibrated assuming it has twice the size and peak output power compared with each PA in the postcombining TX.

To evaluate the effectiveness of compensation throughout the entire power range of the TX, the lower IMD3 term was measured for different input power levels, while the compensation signal was injected as a constant error difference vector according to the scheme in Fig. 3. The correction values were calculated at 9 dBm output power. This was compared with the IMD3 achieved when adapting the correction vector per input power level. The results indicate that the latter practice yields the highest IMD3 suppression [see Fig. 17(b)]. Furthermore, even with the injection of a constant error difference vector, a considerable IMD3 suppression is achieved for all output powers up to 6 dB backoff from the 16 dBm P_{sat} of the PC-TX. We also observe that throughout the entire output power range, the IMD3 of the compensated system is substantially lower than that of a standalone two-tone PA. Table II summarizes the cancellation results of this article compared with previously published works on two-tone measurements of CW signals.

C. OFDM Cancellation Measurements

The measurement setup is shown in Fig. 18. Two OFDM 802.11ac VHT20 signals with 10 dB PAPR were generated in MATLAB and transmitted to the device under test (DUT) at RF from two different ports of the AWG. The compensation signals were equalized based on frequency-flat attenuation and phase shift and injected directly from the other two ports of the AWG. The compensation and the main signals were combined at RF using power combiners in accordance with the scheme of two DACs and RF cancellation path shown in Fig. 3. A Keysight N9040B UXA Spectrum Analyzer and a Keysight DSOS604A VSA were used for the signal reading at the output.

The 2D-DPD algorithm is based on a 2-D vector-piecewise decomposition (2D-VPD) scheme of a precombining TX presented in [27]. Its adaptation to the postcombining TX is straightforward since the learning path does not apply constraints on the source of CM between the two channels. The model parameters were $K = M = 4$, where K and M are
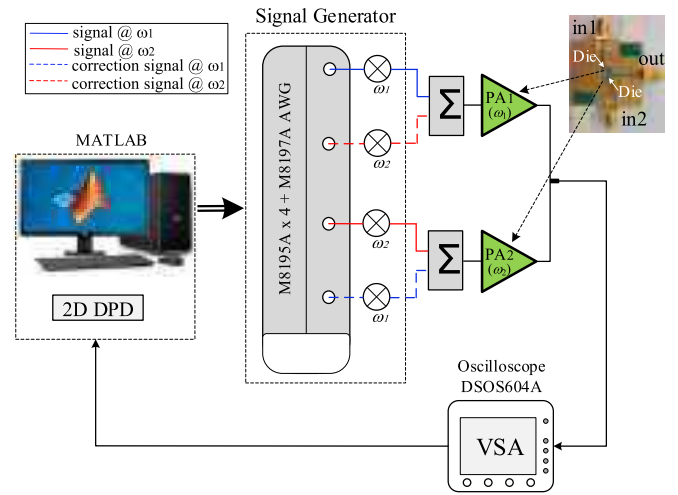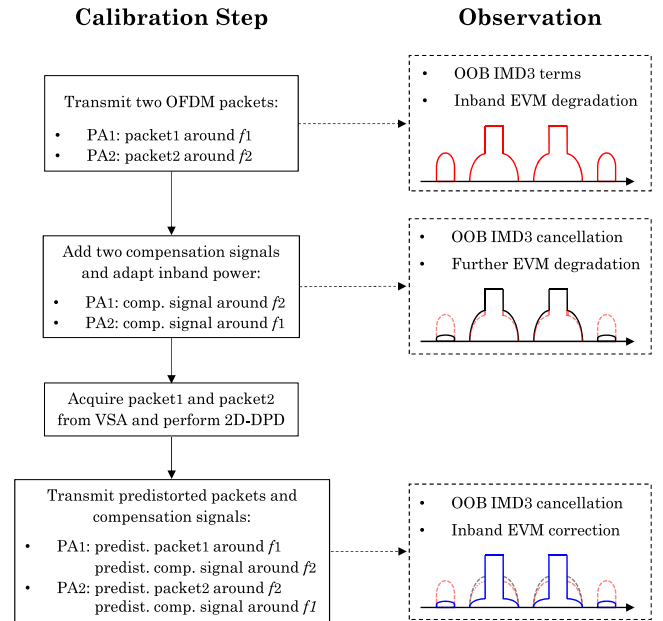

Fig. 18. Measurement setup.

Fig. 19. Calibration procedure.

the nonlinear order and memory length, respectively. A total number of 120 coefficients were used, 60 for each channel. The analog cancellation adds four coefficients per sample if implemented dynamically [corresponding to the green dashed line in Fig. 17(b)]. In cases where the IMD3 suppression target is ~10 dB [green solid line in Fig. 17(b)], the correction coefficients are static and, therefore, do not increase the overall implementation complexity.

The calibration procedure is shown in Fig. 19. Two OFDM packets are transmitted concurrently, and cancellation signals are injected as phase-shifted and attenuated replicas of the fundamental signals to suppress the OOB IMD3 terms. The correction signals generate additional CM distortion, which further increases the in-band spectral regrowth. Finally, the 2D-DPD is applied, considering the original nonlinearities of the TX as well as the excessive CM distortion stemming
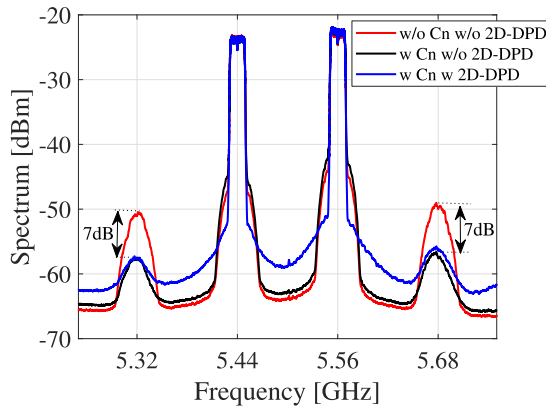
Fig. 20. Measured spectrum and OOB IMD3 suppression of concurrent 20 MHz OFDM signals with 120 MHz frequency separation.
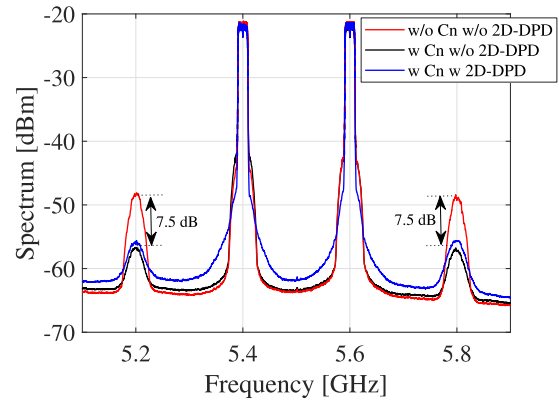
TABLE III
MEASURED EVM IN THE CALIBRATION PROCEDURE

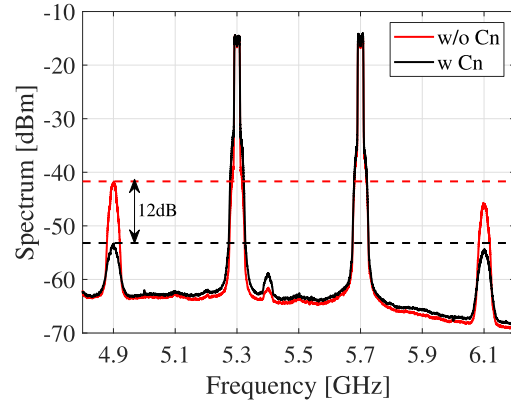| Measurement	5.44 GHz	5.56 GHz
with IMD3 cancellation before DPD	EVM = -24.9 dB P_{out} = 8 dBm	EVM = -24.7 dB P_{out} = 8 dBm
with IMD3 cancellation after DPD	EVM = -31 dB P_{out} = 8 dBm	EVM = -31 dB P_{out} = 8 dBm

from the interaction between the cancellation and the main signals through the PAs' input-referred nonlinearity. The calibration procedure must occur in this order since if 2D-DPD is performed first, it cannot account for the additional CM distortion generated by the correction signals, which will result in error vector magnitude (EVM) degradation as soon as analog cancellation is applied.

Fig. 20 shows the spectrum of the concurrently transmitted packets at the different measurement steps. The analog injection technique suppresses OOB IMD3 by 7 dB, and the 2D-DPD corrects EVM by 6 dB (from −25 to −31 dB). The fifth-order OOB terms (not shown in Fig. 20) are lower than the third-order terms after cancellation. The 4 dB increase in the noise floor is attributed to the PAPR expansion in the DPD and the limited dynamic range of the 8-bit AWG. In order to cope with the higher PAPR, we introduced deliberate clipping to the predistorted signals, which has the effect of the slope observed in the spectrum in-band. The EVM values of this measurement are summarized in Table III.

The same calibration procedure was applied to the above-mentioned signals, but this time with a wider frequency separation of 200 MHz. Analog compensation suppressed OOB IMD3 by 7.5 dB [Fig. 21(a)], and 2D-DPD improved EVM by 7 and 9 dB at the lower and upper frames, respectively. In addition, the compensation technique was tested for wider separation between the carriers to evaluate a scenario in which the OOB IMD3 terms appear outside the transmission band. In this test, DPD was not applied to the main signals. The packets were centered around 5.3 and 5.7 GHz, resulting in OOB IMD3 terms at 4.9 and 6.1 GHz, and 12 dB of total IMD3 cancellation was achieved [see Fig. 21(b)]. The

(a)

(b)

Fig. 21. Measured spectrum and OOB IMD3 cancellation of concurrent 20 MHz OFDM signals. (a) 200 MHz frequency separation. (b) 400 MHz frequency separation.

TABLE IV
OOB IMD3 SUPPRESSION FOR MODULATED SIGNALS

Source	Method	Additional DACs and ADCs	Wideband DAC	Signals BW [MHz]	C/I3* [dBc]	ΔC/I3 [dB]	IMD3 BW [MHz]
Yang [13]	Frequency-Selective DPD	No	Yes	8	45	15	100
Kim [11]	Frequency-Selective DPD	No	Yes	5	55	13	50
Bassam [8]	Channel-Selective DPD	Yes	No	5	36	8	90
This Work	Analog Injection & 2D-DPD	No	No	20	34	7	400
					34	7.5	600
					38	12	1200

deeper suppression of OOB IMD3 may relate to the bandpass behavior of the PA's frequency response [see Fig. 14(b)].

In order to compare the overall linearity of the proposed TX to that of a standalone pre-PA combining two-tone TX, as in Fig. 2-(a1), we combine the suppression in OOB IMD3 terms achieved for modulated signals (see Figs. 20 and 21) with the higher topological linearity characteristics of the postcombining TX (see Fig. 17). We observe

that more than 15 dB reduction in IMD3 levels is achieved, implying that our architecture requires 5 dB less power backoff for similar SFDR, which significantly improves the efficiency performance.

Table IV summarizes the IMD3 cancellation results of this article compared with previously published results in measurements of two modulated signals. The proposed technique achieves comparable cancellation of OOB IMD3 over considerably larger signal BW and channel frequency separation using narrowband DPD and no additional DACs and ADCs.

V. CONCLUSION

A wideband linearization of a two-channel CA TX for widely spaced noncontiguous carriers was proposed and demonstrated with 802.11ac Wi-Fi signals. The TX architecture, together with a unique combination of analog compensation signal injection for OOB IMD3 suppression and 2D-DPD for in-band EVM correction, enables wideband linearization over the entire third-order distortion BW using in-band information solely. This allows the system to make use of the existing narrowband data converters with moderate sampling rates, which is a significant benefit.

The analog cancellation technique is employed in a TX in which two separate PAs are used for two independent Wi-Fi transmissions centered at different carrier frequencies. In order to spare with system resources and allow flexibility in the spectrum utilization, the PAs were connected in parallel to a single antenna, which called for a careful design for the PAs to introduce high output impedance. This reduces mutual loading and mitigates efficiency degradation. The high output impedance characteristic, together with wideband linearization, enables a flexible diplexer-free transmission of two carriers within the aggregated transmission band.

In CW measurements, the linearization technique achieves a spur level of −52 dBc in the compensated post-PA combining system and 30 dB improvement in SFDR compared with a single two-tone PA. OFDM measurements show 7–12 dB of OOB IMD3 cancellation and 6–9 dB improvement in EVM. The standalone PA delivers 17 dBm P_{sat} from a 3.3 V supply and achieves a maximum gain of 16.5 dB and 38% peak PAE. The TX operates around 5.5 GHz with a BW of 1 GHz.

ACKNOWLEDGMENT

REFERENCES

[1] F. M. Ghannouchi, O. Hammi, and M. Helaoui, *Behavioral Modeling and Predistortion of Wideband Wireless Transmitters*. West Sussex, U.K.: Wiley, 2015.

[2] S. A. Bassam, M. Helaoui, and F. M. Ghannouchi, "2-D digital predistortion (2-D-DPD) architecture for concurrent dual-band transmitters," *IEEE Trans. Microw. Theory Techn.*, vol. 59, no. 10, pp. 2547–2553, Oct. 2011.

[3] S. A. Bassam, W. Chen, M. Helaoui, F. M. Ghannouchi, and Z. Feng, "Linearization of concurrent dual-band power amplifier based on 2D-DPD technique," *IEEE Microw. Wireless Compon. Lett.*, vol. 21, no. 12, pp. 685–687, Dec. 2011.

[4] R. N. Braithwaite, "Digital predistortion of a power amplifier for signals comprising widely spaced carriers," in *Proc. 78th ARFTG Microw. Meas. Conf.*, Dec. 2011, pp. 1–4.

[5] M. Cabarkapa, N. Neskovic, and D. Budimir, "A generalized 2-D linearity enhancement architecture for concurrent dual-band wireless transmitters," *IEEE Trans. Microw. Theory Techn.*, vol. 61, no. 12, pp. 4579–4590, Dec. 2013.

[6] W. Chen, X. Chen, S. Zhang, and Z. Feng, "Energy-efficient concurrent dual-band transmitter for multistandard wireless communications," in *Proc. Asia–Pacific Microw. Conf.*, Nov. 2014, pp. 558–560.

[7] M. Cabarkapa, N. Neskovic, and D. Budimir, "2-D nonlinearity compensation technique for concurrent dual-band wireless transmitters," in *IEEE MTT-S Int. Microw. Symp. Dig.*, Jun. 2013, pp. 1–3.

[8] S. A. Bassam, M. Helaoui, and F. M. Ghannouchi, "Channel-selective multi-cell digital predistorter for multi-carrier transmitters," *IEEE Trans. Commun.*, vol. 60, no. 8, pp. 2344–2352, Aug. 2012.

[9] P. Roblin *et al.*, "Frequency-selective predistortion linearization of RF power amplifiers," *IEEE Trans. Microw. Theory Techn.*, vol. 56, no. 1, pp. 65–76, Jan. 2008.

[10] M. Abdelaziz, L. Anttila, A. Mohammadi, F. Ghannouchi, and M. Valkama, "Reduced-complexity power amplifier linearization for carrier aggregation mobile transceivers," in *Proc. IEEE Int. Conf. Acoust., Speech Signal Process. (ICASSP)*, May 2014, pp. 3908–3912.

[11] J. Kim, P. Roblin, D. Chaillot, and Z. Xie, "A generalized architecture for the frequency-selective digital predistortion linearization technique," *IEEE Trans. Microw. Theory Techn.*, vol. 61, no. 1, pp. 596–605, Jan. 2012.

[12] S. Lajnef, N. Boulejfen, and F. M. Ghannouchi, "Linearization of a concurrent dual-band transmitter exhibiting nonlinear distortion and hardware impairments using baseband injection," in *Proc. 7th Int. Conf. Sci. Electron., Technol. Inf. Telecommun. (SETIT)*, Dec. 2016, pp. 361–364.

[13] X. Yang *et al.*, "Fully orthogonal multi-carrier predistortion linearization for RF power amplifiers," in *IEEE MTT-S Int. Microw. Symp. Dig.*, Jun. 2009, pp. 1077–1080.

[14] R. N. Braithwaite, "Using a cascade of digital and analog predistortion to linearize a dual-band RF transmitter," in *Proc. IEEE Top. Conf. RF/Microw. Power Modeling Radio Wireless Appl. (PAWR)*, Jan. 2017, pp. 77–80.

[15] P. C. Chun, C. H. Chan, and Q. Xue, "Dual baseband injection method for amplifier linearization," in *Proc. Asia–Pacific Microw. Conf.*, Dec. 2007, pp. 1–3.

[16] D. Jing, W. Shing Chan, S. Man Li, and C. Wai Li, "New linearization method using interstage second harmonic enhancement," *IEEE Microw. Guided Wave Lett.*, vol. 8, no. 11, pp. 402–404, Nov. 1998.

[17] M. R. Moazzam and C. S. Aitchison, "A low third order intermodulation amplifier with harmonic feedback circuitry," in *IEEE MTT-S Int. Microw. Symp. Dig.*, vol. 2, Jun. 1996, pp. 827–830.

[18] Y. Yang and B. Kim, "A new linear amplifier using low-frequency second-order intermodulation component feedforwarding," *IEEE Microw. Guided Wave Lett.*, vol. 9, no. 10, pp. 419–421, Oct. 1999.

[19] C.-W. Fan and K.-K.-M. Cheng, "Theoretical and experimental study of amplifier linearization based on harmonic and baseband signal injection technique," *IEEE Trans. Microw. Theory Techn.*, vol. 50, no. 7, pp. 1801–1806, Jul. 2002.

[20] S. Bulja and D. Mirshekar-Syahkal, "Combined low frequency and third harmonic injection in power amplifier linearization," *IEEE Microw. Wireless Compon. Lett.*, vol. 19, no. 9, pp. 584–586, Sep. 2009.

[21] N. Ginzberg, D. Regev, G. Tsodik, S. Shilo, D. Ezri, and E. Cohen, "A 5GHz to 6GHz CMOS transmitter for full-duplex wireless with wideband digital cancellation," in *Proc. IEEE Radio Freq. Integr. Circuits Symp. (RFIC)*, Jun. 2019, pp. 87–90.

[22] N. Ginzberg, Y. Schwartz, and E. Cohen, "Linearization technique of diplexer-free transmitter for carrier aggregation signals," in *Proc. IEEE Int. Conf. Microw., Antennas, Commun. Electron. Syst. (COMCAS)*, Nov. 2017, pp. 1–4.

[23] J. C. Pedro and J. Perez, "Accurate simulation of GaAs MESFET's intermodulation distortion using a new drain-source current model," *IEEE Trans. Microw. Theory Techn.*, vol. 42, no. 1, pp. 25–33, Jan. 1994.

[24] S. A. Maas, *Nonlinear Microwave Circuits*. Norwood, MA, USA: Artech House, 1988.

[25] N. Males-Ilic, B. Milovanovic, and D. Budimir, "Linearization technique for reducing third-and fifth-order intermodulation distortion products in multichannel amplifiers," in *Proc. 33rd Eur. Microw. Conf.*, Oct. 2003, pp. 1235–1238.

[26] D. Chowdhury, C. D. Hull, O. B. Degani, Y. Wang, and A. M. Niknejad, "A fully integrated dual-mode highly linear 2.4 GHz CMOS power amplifier for 4G WiMax applications," *IEEE J. Solid-State Circuits*, vol. 44, no. 12, pp. 3393–3402, Dec. 2009.

[27] T. Gidoni, E. Cohen, and E. Socher, "Digital predistortion on concurrent noncontiguous transmitters using 2D piecewise vector decomposition," in *Proc. IEEE Int. Conf. Microw., Antennas, Commun. Electron. Syst. (COMCAS)*, Nov. 2017, pp. 1–5.

Yanir Schwartz received the B.Sc. degree in electrical engineering from the Technion—Israel Institute of Technology, Haifa, Israel, in 2015, where he is currently pursuing the M.Sc. degree in electrical engineering.

His research focuses on transmitter–receiver isolation techniques for frequency-division duplexed phased arrays at millimeter-wave frequencies.

Nimrod Ginzberg (Graduate Student Member, IEEE) received the B.Sc. degree in electrical engineering, the B.A. degree in physics, and the M.Sc. degree from the Technion—Israel Institute of Technology, Haifa, Israel, in 2015, 2015, and 2017, respectively, where he is currently pursuing the Ph.D. degree in electrical engineering.

His current research interests include full-duplex and carrier aggregation transmitters for 5G wireless communication systems.

Tomer Gidoni received the M.Sc. degree in electrical engineering from Tel Aviv University, Tel Aviv, Israel, in 2020. His research thesis focused on 2-D piecewise linearization algorithms for concurrent transmitters.

In 2012, he joined the Wireless Communication Solutions (WCS) Group, Intel, Petah Tikva, Israel, where he works as an RF Architect covering cross-domain and multidiscipline topics, responsible for Wi-Fi frequency generation and BT receiver architectures. His current research interests include integrated transceiver and frequency generation architectures and system modeling in CMOS technology.

Emanuel Cohen (Member, IEEE) received the B.Sc. degree in electrical engineering, the M.Sc. degree, and the Ph.D. degree in electrical engineering from the Technion—Israel Institute of Technology, Haifa, Israel, in 1996, 2002, and 2012, respectively.

His research areas include millimeter-wave phased array in advanced CMOS process and high-speed mixed-signal for power efficiency. He worked nine years on military communication systems as the Head of the RF Department. In 2004, he joined Intel, Petah Tikva, Israel, where he was involved with Wi-Fi and WiMAX systems, defining and developing the RF integrated circuits (RFICs) and algorithms for these standards, including calibrations for BIST systems, linearization, and efficiency enhancement for power amplifiers. Since 2015, he has been an Assistant Professor with the Technion—Institute of Technology.